

Quantized anomalous Hall resistivity achieved in molecular beam epitaxy-grown MnBi₂Te₄ thin films

Yunhe Bai^{1*}, Yuanzhao Li^{1*}, Jianli Luan^{1*}, Ruixuan Liu^{1*}, Wenyu Song¹, Yang Chen¹, Peng-Fei Ji¹, Qinghua Zhang⁷, Fanqi Meng⁶, Bingbing Tong³, Lin Li³, Yuying Jiang¹, Zongwei Gao³, Lin Gu⁶, Jinsong Zhang^{1,2,5}, Yayu Wang^{1,2,5}, Qi-Kun Xue^{1,2,3,4}, Ke He^{1,2,3,5†}, Yang Feng^{3†}, and Xiao Feng^{1,2,3,5†}

¹*State Key Laboratory of Low Dimensional Quantum Physics, Department of Physics, Tsinghua University, Beijing 100084, China*

²*Frontier Science Center for Quantum Information, Beijing 100084, China*

³*Beijing Academy of Quantum Information Sciences, Beijing 100193, China*

⁴*Southern University of Science and Technology, Shenzhen 518055, China*

⁵*Hefei National Laboratory, Hefei 230088, China*

⁶*School of Materials Science and Engineering, Tsinghua University, Beijing 100084, China*

⁷*Institute of Physics, Chinese Academy of Sciences, Beijing 100190, China*

* *These authors contributed equally to this work.*

† *Corresponding author. Email: kehe@tsinghua.edu.cn (K. H.); fengyang@baqis.ac.cn (Y. F.); xiaofeng@mail.tsinghua.edu.cn (X. F.)*

Abstract

The intrinsic magnetic topological insulator MnBi₂Te₄ provides a feasible pathway to high temperature quantum anomalous Hall (QAH) effect as well as various novel topological quantum phases. Although quantized transport properties have been observed in exfoliated MnBi₂Te₄ thin flakes, it remains a big challenge to achieve molecular beam epitaxy (MBE)-grown MnBi₂Te₄ thin films even close to the quantized regime. In this work, we report the realization of quantized anomalous Hall resistivity in MBE-grown MnBi₂Te₄ thin films with the chemical potential tuned by both controlled in-situ oxygen exposure and top gating. We find that elongated post-annealing obviously elevates the temperature to achieve quantization of the Hall resistivity, but also increases the residual longitudinal resistivity, indicating a picture of high-quality QAH puddles weakly coupled by tunnel barriers. These results help to clarify the puzzles in previous experimental studies on MnBi₂Te₄ and to find a way out of the big difficulty in obtaining MnBi₂Te₄ samples showing quantized transport properties.

Introduction

The quantum anomalous Hall (QAH) effect is a quantum Hall (QH) effect induced by spontaneous magnetization of a material and thus free from external magnetic field [1]. After the first experimental realization in molecular beam epitaxy (MBE)-grown thin films of a magnetically doped topological insulator (TI) in 2013 [2], the QAH effect has attracted rapidly growing research interests as a route towards various other exotic quantum phases such as axion insulator and chiral topological superconductor [3,4]. Magnetically doped TIs need a rather low temperature (usually below 1 K) to exhibit the QAH effect and are highly disordered due to the randomly distributed magnetic dopants [5,6]. In recent years, two kinds of intrinsic QAH systems have been discovered, namely, thin films/flakes of MnBi_2Te_4 -family compounds [7–11] and moiré superlattices of two-dimensional (2D) materials [12–14], providing potentially cleaner and more robust alternatives to magnetically doped TIs. Particularly, the huge magnetic gap predicted in MnBi_2Te_4 films (~ 50 meV) heralds a high temperature QAH effect. Nearly quantized transport properties have indeed been observed in MnBi_2Te_4 thin flake samples up to ~ 40 K [15]. However, MnBi_2Te_4 thin flakes (also moiré superlattices) rely on rather challenging and tricky fabrication techniques, and suffer from the irregular shape, small size, and ill-controlled performance of the samples. Actually, only a few groups world-wide have ever succeeded in obtaining MnBi_2Te_4 flakes showing quantized transport properties at a rather low yield even with the best single crystals. The intractable thin flake samples make systematic studies and optimizations very difficult, leading to seemingly inconsistent data from different samples and measurements [11,15–20]. Moreover, to explore QAH-based novel topological quantum states [21,22] and their electronic applications, MnBi_2Te_4 samples should be prepared in a repeatable, controllable and scalable way so that they can construct complex and large-area heterostructures, arrays and circuits for different purposes. It is very difficult for thin flake samples to satisfy the requirement.

Molecular beam epitaxy can provide large, regular and well-controlled samples with excellent repeatability and tunability, particularly advantageous in scalable

preparation of QAH-based heterostructures. Although MBE growth of MnBi_2Te_4 thin films has long since been achieved, the largest Hall resistivity obtained in those samples merely reached half of the quantized value (h/e^2) so far [10,23–27]. In this work, we achieved MBE-grown MnBi_2Te_4 thin films showing quantized Hall resistivity in the ferromagnetic (FM) configuration under high magnetic field. The much larger sample size and higher repeatability of sample properties enable us to systematically study their properties and clarify some puzzles in previous works on MnBi_2Te_4 .

Results and discussion

The schematic procedure of sample preparation is shown in Fig. 1a. MnBi_2Te_4 films are grown on sapphire (0001) substrates by co-evaporation of Mn, Bi and Te and post-annealing at 270°C (see Methods, SI A and ref. [28] for the detailed MBE growth procedure and parameters). Figure 1b shows the reflection high energy electron diffraction (RHEED) pattern of a MnBi_2Te_4 film (the inset is that for the sapphire substrate). The as-grown MnBi_2Te_4 films are electron-doped due to unavoidable occupying of Bi atoms on Mn sites [29], similar to single crystal samples. We apply in-situ oxygen exposure and electric gating to coarsely and finely tune the Fermi level into the surface state gap, respectively [30]. The as-grown films are transferred to another chamber of the same MBE system and exposed to $\sim 1 \times 10^{-3}$ mbar O_2 for an hour at room temperature. The pressure resembles the O_2 partial pressure in a glove box for exfoliating MnBi_2Te_4 flakes. The oxygen pressure is slightly modified for samples of different thicknesses to keep them roughly charge neutral. Such a medium O_2 exposure effectively reduces the carrier density of MnBi_2Te_4 films with little influence to their electronic structures and properties (Figs. S2 and S3). After O_2 exposure, an 8-nm-thick cadmium selenide (CdSe) capping layer is deposited onto the films to avoid uncontrolled charge doping in the following fabrications and measurements. The atomic force microscopy and high-resolution scanning transmission electron microscopy (STEM) images of a nominally five-septuple-layer (5-SL) MnBi_2Te_4 sample with CdSe capping layer are shown in Figs. 1c and 1d, respectively. The film is mainly composed of one terrace of uniform thickness, distributed with small islands

and depressions of 1-SL height.

The MnBi_2Te_4 films are lithographed by argon ion milling into Hall bars ($40 \mu\text{m} \times 80 \mu\text{m}$) through a molybdenum mask. An AlO_x dielectric layer is then grown on the samples by atomic layer deposition, and the top-gate electrode is deposited on it through another molybdenum mask (the upper limit of the sample size is determined by the quality of the dielectric layer). The false-color photo of a final device is displayed in Fig. 1e. The sample temperature is kept below 60°C during the whole top-gate structure fabrication procedure to avoid sample degradation. The low temperature tolerance may come from the oxygen introduced in the films. Different devices on a $3 \text{ mm} \times 5 \text{ mm}$ sample show similar transport properties (Fig. S9), indicating the excellent homogeneity and repeatability of the MBE-grown MnBi_2Te_4 samples. Figure 1f displays the longitudinal resistivity (ρ_{xx})–temperature (T) curve of a 5-SL MnBi_2Te_4 thin film (with the gate voltage $V_g = 0 \text{ V}$), which exhibits a clear cusp at 21.8 K corresponding to the Néel temperature (T_N) and an insulating behavior at lower temperature [31,32].

Figures 2a and 2b show the magnetic field ($\mu_0 H$) dependences of the Hall (ρ_{yx}) and longitudinal (ρ_{xx}) resistivities, respectively, of a 5-SL sample (at charge-neutral point) measured at five different temperatures. Figure 2c displays the $\rho_{yx}-V_g$ and $\rho_{xx}-V_g$ curves at $T = 0.02 \text{ K}$ and $\mu_0 H = -9 \text{ T}$. The sample was post-annealed at 270°C for 30 min. after MBE growth (referred below as 5 SL-1). The $\rho_{yx}-\mu_0 H$ and $\rho_{xx}-\mu_0 H$ curves have the typical shapes of MnBi_2Te_4 : the high field ($> 6.5 \text{ T}$) and low field ($< 3 \text{ T}$) parts of the curves roughly correspond to MnBi_2Te_4 in the FM and antiferromagnetic (AFM) configurations, respectively. In the FM state around $\pm 9 \text{ T}$, $|\rho_{yx}|$ and ρ_{xx} always evolve inversely, with magnetic field, gate voltage and temperature, which is a signature of the dissipationless quantum Hall or QAH edge state. The former one is excluded by the absent transport evidence of Landau levels, such as Shubnikov de Haas (SdH) peaks. Therefore, the QAH state dominates the high-field transport properties. At 0.02 K , $|\rho_{yx}|$ reaches $0.98h/e^2$, and ρ_{xx} drops to $0.20h/e^2$ at $\pm 9 \text{ T}$, exhibiting a decent quantization. Descendible deviation of ρ_{yx} from quantization is observed at 0.4 K ($0.93h/e^2$). It is

difficult to accurately estimate the activation gap from the $\sigma_{xx}-T^{-1}$ curve (Fig. S14). But according to Figs. 2a and 2b, the gap size should be at the same level as that of Cr-doped $(\text{Bi,Sb})_2\text{Te}_3$ films, much lower than that of good MnBi_2Te_4 flake samples. In the AFM state at low field (between ± 3 T), the $\rho_{yx}-\mu_0H$ curves exhibit a hysteresis loop, with the coercive field (H_c) of ~ 1.1 T and zero field ρ_{yx} of $\sim 0.34h/e^2$ at 0.02 K (Fig. 2a). ρ_{xx} at high field decreases with decreasing temperature, as expected in a QAH system, meanwhile at low field, ρ_{xx} increases with decreasing temperature, showing an insulating behavior (Fig. 2b).

We systematically investigate thickness-dependent transport properties of the MnBi_2Te_4 films from 2 SL to 7 SL, all post-annealed at 270°C for 30 min, as shown in Fig. S5. The 4-SL to 6-SL samples all show a nearly quantized ρ_{yx} and a ρ_{xx} minimum at high field in both the μ_0H - and V_g -dependent curves, indicating the QAH states in the FM state. No signatures of the QAH state are observed in the 2-SL and 3-SL films. The absence of the QAH state in the 3-SL film, which ought to be in the QAH regime according to early works [7,11], may be attributed to the influence of oxidation [33]. In the 7-SL film, the signatures of the QAH state can hardly be distinguished due to parallel conduction channels.

We found that elongated post-annealing significantly changes the transport properties of the films. Figures 2d and 2e display the $\rho_{yx}-\mu_0H$ and $\rho_{xx}-\mu_0H$ curves, respectively, of a 5-SL MnBi_2Te_4 film with post-annealing at 270°C for 120 min. (referred as 5 SL-2) measured at different temperatures. The annealing was carried out in Te flux to avoid Te desorption. Notably, $|\rho_{yx}|$ of the sample reaches full quantization ($0.99h/e^2$) at 0.02 K at high field (the strong noise in the $\rho_{yx}-\mu_0H$ curve between ± 5 T is due to the huge ρ_{xx} , which will be discussed below). The Hall resistivity keeps $0.98h/e^2$ at 0.4 K, $0.97h/e^2$ at 0.7 K, and still $0.89h/e^2$ even at 2 K. Obviously, the ρ_{yx} quantization at high field becomes more robust to temperature, comparable to some MnBi_2Te_4 thin flake samples. On the other hand, ρ_{xx} is significantly enhanced, rather than reduced as expected in a good QAH sample, by the elongated annealing. The high-field ρ_{xx} of the sample is $0.73h/e^2$ at ± 9 T, 0.02 K, and rises with increasing temperature, suggesting

that the ground state is still the QAH phase. The low field ρ_{xx} at 0.02 K becomes extremely large (the measured ρ_{xx} of $\sim 200h/e^2$ is not accurate due to the too large resistance), and drops rapidly with increasing temperature (about $5h/e^2$ even at 2 K), exhibiting a typical insulating behavior. It suggests absence of dissipationless chiral edge states in the sample at low field, which will be discussed later.

The effect of annealing duration can be clearly seen in the $\rho_{yx}-V_g$ and $\rho_{xx}-V_g$ curves measured at -9 T and 0.02 K of the 5 SL-1 (Fig. 2c) and 5 SL-2 (Fig. 2f) samples, and also in their temperature dependences of ρ_{yx} (Fig. 3a) and ρ_{xx} (Fig. 3b) at -9 T. Obviously, elongated annealing drives ρ_{yx} closer to the quantized value (h/e^2) but makes ρ_{xx} farther away from zero at high field. Longer post-annealing duration time (at 270°C) does not obviously change the sample properties further, as shown in Fig. 3c. So 120 min. post-annealing is selected representatively. Similar annealing effect is also observed in the films of other thicknesses (Fig. S14).

In a well quantized QAH film, the dissipationless chiral edge channel surrounding the whole sample contributes to quantized ρ_{yx} and vanishing ρ_{xx} (see Fig. 3e). With dissipative conduction channels of residual bulk carriers, ρ_{xx} becomes non-zero, and ρ_{yx} drops below the quantized value (Fig. 3f). The early results on the QAH effect and the data of the MnBi_2Te_4 film with 30 min. annealing (Figs. 2a and 2b) are all consistent with this case. It thus looks confusing that the sample with 120 min. annealing has a perfectly quantized ρ_{yx} below 0.4 K but, at the same time, keeps a large ρ_{xx} at high field (Figs. 2d and 2e). The quantized ρ_{yx} accompanied by a significant ρ_{xx} was ever observed and discussed in two-dimensional electron systems, known as the “quantized Hall insulator”, which is composed of weakly coupled quantum Hall regions (puddles) [34], each surrounded by dissipationless quantum Hall edge states. The tunneling between the neighboring quantum Hall puddles contributes to a large ρ_{xx} of the whole sample which is determined by the transmission probability (Fig. 3g) [35], meanwhile ρ_{yx} can still remain the quantized value. Although the MnBi_2Te_4 films with elongated annealing have a QAH ground state at high field, not really an insulator, the high residual ρ_{xx} can be understood with this picture. Namely, the samples are composed of well-quantized

QAH puddles with the tunneling between the puddles giving a large ρ_{xx} of the whole sample.

Through ordinary Hall effect measurements above T_N , we found that the MnBi_2Te_4 films with longer-time post-annealing have a lower carrier density at the charge-neutral point (Fig. 3d). Probably, long-time annealing aggregates the defects or impurities that induce the chemical potential fluctuation in a MnBi_2Te_4 film [36], e.g. Mn atoms occupying Bi sites. As a result, most areas of the film become cleaner with less chemical potential fluctuations, acting as high-quality QAH puddles. But at their boundaries where defects aggregate, the QAH phases are destroyed, and the dissipationless edge states of QAH puddles can only tunnel through there, contributing to the non-zero ρ_{xx} . Therefore, the residual ρ_{xx} is expected to be reduced in MnBi_2Te_4 films of smaller size which includes fewer QAH puddles. Our preliminary result indeed shows that a MnBi_2Te_4 device of smaller size exhibits a lower ρ_{xx} under high field than a device of larger size (Fig. S12), while a systematic size-dependent transport study is needed to confirm it. Similar situation may also happen in MnBi_2Te_4 single crystals which usually experience a rather long-time annealing. Consequently, full quantization is observed in exfoliated thin flakes (usually several μm large) only including clean areas, but not in those with aggregated defects. It explains the low yield of MnBi_2Te_4 thin flake samples showing perfect quantized transport properties.

Figures 4a and 4b display the $\mu_0 H$ dependences of the longitudinal (σ_{xx}) and Hall (σ_{xy}) conductivities measured at different temperatures of the 5-SL films with 30 min. and 120 min. post-annealing, respectively. At high field, the former sample has nearly quantized σ_{xy} , meanwhile the latter one has σ_{xy} obviously lower than e^2/h due to the larger ρ_{xx} , despite the fully quantized ρ_{yx} . The ground states of the films can be checked by the tendency of the conductivity tensor (σ_{xy} , σ_{xx}) evolution with increasing magnetic field and decreasing temperature (the flow charts), as shown in Fig. 4c. Here, the data of 5-SL, 6-SL and 7-SL films are plotted, and the left and right parts correspond to the data from the long- and short-time post-annealed samples, respectively. Similar to early results of the quantum Hall and QAH effects [37–40], the conductivity tensors tend to

flow towards $(0, 0)$ or $(e^2/h, 0)$ points at low temperature. The $(0, 0)$ point is the insulating phase (also known as the Hall insulator), and the $(e^2/h, 0)$ point is the QAH or quantum Hall phases [41–44].

In the FM configuration (high field), the conductivity tensors of the films all flow towards the $(e^2/h, 0)$ points with increasing magnetic field (indicated by the black arrow) and decreasing temperature, which indicates a QAH ground state (the quantum Hall phase is excluded as discussed above). In the AFM configuration (low field), the conductivity tensors all flow to the $(0, 0)$ point with decreasing magnetic field (the opposite direction of the black arrow) and temperature, regardless of odd- or even-SL films, which indicates an insulating ground state as directly observed in Figs. 2b and 2e. The $\rho_{xx}-\mu_0H$ curves of the two 5-SL samples measured at different temperatures all cross at one point, signifying a quantum phase transition from the QAH state (high field) to the insulating state (low field). A scaling analysis near the critical magnetic field (H_{cr}) is shown in the insets of Figs. 4d and 4e, where the relation between ρ_{xx} and the scaling variable $(H-H_{cr})/T^\kappa$ are plotted. ρ_{xx} collapses into two branches contributed by two sides of H_{cr} , respectively, with the fitted scaling exponent $\kappa = 0.45$, identical to that for the phase transitions in QH systems [45].

The insulating behavior in the odd-SL films at low field looks inconsistent with the prediction that MnBi_2Te_4 in the AFM configuration is a Chern insulator in the odd-SL films [7–9]. One possible cause is the thickness fluctuations of films. The 1-SL islands and depressions as shown in Fig. 1c make an odd-SL QAH film mixed with even-SL axion insulator regions, which could elevate ρ_{xx} . However, according to early theoretical and experimental results on magnetically modulation-doped TI films [46], even when half of a QAH film becomes axion insulator, ρ_{xx} only increases to $\sim 1h/e^2$ which is much lower than the observed ρ_{xx} of up to hundreds h/e^2 in the MnBi_2Te_4 films with 120 min. annealing. Actually, we found that the measured ρ_{xx} of odd-SL films is not sensitive to the coverage of the even-SL regions (Fig. S13). The zero-magnetic-field insulating state has also been reported in many odd-SL MnBi_2Te_4 flakes that show quantized ρ_{yx} at high field, without thickness fluctuation [15,17,19,47]. The

conductivity tensor data of MnBi_2Te_4 thin flakes at zero field around 1.5 K are also plotted in Fig. 4c for comparison. Most of the data are near the (0, 0) point, suggesting an insulating ground state. The insulating ground state is confirmed by the huge resistivity observed in our MBE films. Only in very rare odd-SL flake samples, has the QAH effect at zero magnetic field been observed [11].

Another possibility is that many AFM domains exist in the films around zero magnetic field, instead of the single AFM domain case assumed by the theoretical work predicting the QAH effect. Antiferromagnetic domains have been observed in MnBi_2Te_4 single crystals by magnetic force microscopy with the typical size of $\sim 10 \mu\text{m}$ [48,49]. Since the domain size is much larger than the width of the QAH edge states in MnBi_2Te_4 ($\sim 1 \mu\text{m}$) [20], the sample can be considered as a network of chiral edge states, which usually gives a ρ_{xx} of the same order of magnitude as h/e^2 [50,51]. Again, the huge ρ_{xx} observed in the samples with 120 min. annealing suggests absence of the chiral edge state network. However, the magnetic structure of the MnBi_2Te_4 thin films/flakes might be different from single crystals due to the low thickness. There are other possibilities, e.g. the influences of antisite defects [52], that might also lead to the insulating behavior in MnBi_2Te_4 thin films/flakes at zero field. The present data are not enough to decide which mechanism dominates. Nevertheless, the huge ρ_{xx} at zero magnetic field and its sensitivity to the post-annealing condition may help to understand the large fluctuations in sample properties of MnBi_2Te_4 thin flakes. Besides, considering that the QAH state is probably absent in most MnBi_2Te_4 samples at zero magnetic field, whatever the reason is, it is reasonable that previous angle-resolved photoemission spectroscopy (ARPES) measurements on MnBi_2Te_4 (on large samples at zero magnetic field) failed to clearly demonstrate the magnetic gap opening as predicted theoretically [22].

Conclusion

In summary, we have achieved MBE-grown MnBi_2Te_4 thin films exhibiting quantized Hall resistivity at high magnetic field. Both even- and odd-SL films show insulating behavior around zero magnetic field. Elongating the post-annealing time is

found to significantly enhance the temperature to reach ρ_{yx} quantization (at high field), but at the same time increase the residual ρ_{xx} , indicating formation of QAH puddles with their chiral edge states tunneled with each other. The information obtained from the MBE-grown films with good repeatability may help to clarify the complexity in the experimental results on MnBi_2Te_4 and improve the material for explorations to high temperature QAH effect and other novel topological quantum effects.

Methods

Thin film growth

MnBi_2Te_4 thin films are grown on treated sapphire (0001) substrates in an ultrahigh-vacuum MBE system with base pressure better than 2.0×10^{-10} mbar. The commercial substrates are annealed in a tube furnace at 1100°C for 3 hours under O_2 atmosphere to obtain flat terraces on the surfaces. The treated substrates are degassed at 400°C for 30 minutes before growth. High purity Mn (99.9998%), Bi (99.9999%) and Te (99.9999%) are co-evaporated with commercial Knudsen cells. Post-annealing process at growth temperature for 0.5~10 hours is implemented to further improve sample quality. (If the annealing time is longer than 2 hours, Te flux is applied to avoid Te desorption.) After growth, the samples are in-situ exposed to oxygen with different pressures for different thicknesses and then an 8-nm CdSe layer is capped on the top at room temperature. Before the following fabrication, the topography is scanned by atomic force microscopy (Bruker, Innova). See more details in SI A.

Fabrication

The MnBi_2Te_4 films are lithographed by argon ion milling into Hall bars ($40 \mu\text{m} \times 80 \mu\text{m}$) through a molybdenum mask. Then, a 40-nm AlO_x layer is grown on the samples as a gate dielectric by atomic layer deposition. The top-gate electrode of 5 nm Ti/ 20 nm Au is deposited on it through another molybdenum mask. Indium is applied as Hall bar electrodes.

Transport measurements

Magneto-transport measurements are performed in a commercial dilution fridge Oxford Instrument Triton 400 with a base temperature below 20 mK. Due to the large resistance at low temperature, we use delta mode, combining source meter and voltmeter. The DC current is applied by the digital

source meter Keithley 6221. The voltage drop is measured by the voltmeter Keithley 2182A. At low temperature, the delay time between the start of DC current applied and voltage reading is from 1.6 s to 5.1 s for different samples. The longitudinal and Hall voltage drops V_{xx} and V_{yx} are detected separately in different magnetic field sweeps. For samples 5 SL-1, 6 SL-1 and 7 SL-1, the source-drain currents used in longitudinal (I_{xx}) and Hall (I_{yx}) measurements are both 1 nA. For samples 4 SL, 5 SL-2, 6 SL-2 and 7 SL-2, I_{xx} and I_{yx} are 1 nA and 10 nA, respectively. The current remains unchanged during the variation of temperature and gating. The top gate (AlO_x dielectric) voltages are applied by a Keithley 2400 multimeter.

Acknowledgements

We thank C. Liu for helpful discussions. We thank Q. Liu for his help with device fabrications. We also thank Z. Li and C. Guo for their help with ToF-SIMS measurements.

Funding

This work was supported by the National Natural Science Foundation of China (92065206, 11904053), the National Key Research and Development Program of China (2018YFA0307100, 2017YFA0303303), the Innovation Program for Quantum Science and Technology (2021ZD0302502).

References

1. Liu CX, Zhang SC and Qi XL. The quantum anomalous Hall effect: theory and experiment. *Annu Rev Condens Matter Phys* 2016; **7**: 301–21.
2. Chang CZ, Zhang J and Feng X *et al.* Experimental observation of the quantum anomalous Hall effect in a magnetic topological insulator. *Science* 2013; **340**: 167–70.
3. Qi XL and Zhang SC. Topological insulators and superconductors. *Rev Mod Phys* 2011; **83**: 1057–110.
4. Sekine A and Nomura K. Axion electrodynamics in topological materials. *J Appl Phys* 2021; **129**: 141101.
5. Mogi M, Yoshimi R and Tsukazaki A *et al.* Magnetic modulation doping in topological insulators toward higher-temperature quantum anomalous Hall effect. *Appl Phys Lett* 2015; **107**: 182401.

6. Ou Y, Liu C and Jiang G *et al.* Enhancing the quantum anomalous Hall effect by magnetic codoping in a topological insulator. *Adv Mater* 2018; **30**: 1703062.
7. Otrokov MM, Rusinov IP and Blanco-Rey M *et al.* Unique thickness-dependent properties of the van der Waals interlayer antiferromagnet MnBi_2Te_4 films. *Phys Rev Lett* 2019; **122**: 107202.
8. Li J, Li Y and Du S *et al.* Intrinsic magnetic topological insulators in van der Waals layered MnBi_2Te_4 -family materials. *Sci Adv* 2019; **5**: eaaw5685.
9. Zhang D, Shi M and Zhu T *et al.* Topological axion states in the magnetic insulator MnBi_2Te_4 with the quantized magnetoelectric effect. *Phys Rev Lett* 2019; **122**: 206401.
10. Gong Y, Guo J and Li J *et al.* Experimental realization of an intrinsic magnetic topological insulator. *Chin Phys Lett* 2019; **36**: 076801.
11. Deng Y, Yu Y and Shi MZ *et al.* Quantum anomalous Hall effect in intrinsic magnetic topological insulator MnBi_2Te_4 . *Science* 2020; **367**: 895–900.
12. Chen G, Sharpe AL and Fox EJ *et al.* Tunable correlated Chern insulator and ferromagnetism in a moiré superlattice. *Nature* 2020; **579**: 56–61.
13. Serlin M, Tschirhart CL and Polshyn H *et al.* Intrinsic quantized anomalous Hall effect in a moiré heterostructure. *Science* 2020; **367**: 900–3.
14. Li T, Jiang S and Shen B *et al.* Quantum anomalous Hall effect from intertwined moiré bands. *Nature* 2021; **600**: 641–6.
15. Ge J, Liu Y and Li J *et al.* High-Chern-number and high-temperature quantum Hall effect without Landau levels. *Natl Sci Rev* 2020; **7**: 1280–7.
16. Liu C, Wang Y and Li H *et al.* Robust axion insulator and Chern insulator phases in a two-dimensional antiferromagnetic topological insulator. *Nat Mater* 2020; **19**: 522–7.
17. Ovchinnikov D, Huang X and Lin Z *et al.* Intertwined topological and magnetic orders in atomically thin Chern insulator MnBi_2Te_4 . *Nano Lett* 2021; **21**: 2544–50.
18. Gao A, Liu YF and Hu C *et al.* Layer Hall effect in a 2D topological axion antiferromagnet. *Nature* 2021; **595**: 521–5.
19. Ying Z, Zhang S and Chen B *et al.* Experimental evidence for dissipationless transport of the chiral edge state of the high-field Chern insulator in MnBi_2Te_4 nanodevices. *Phys Rev B* 2022; **105**: 085412.
20. Lin W, Feng Y and Wang Y *et al.* Direct visualization of edge state in even-layer MnBi_2Te_4 at zero magnetic field. *Nat Commun* 2022; **13**: 7714.

21. Wang J, Zhou Q and Lian B *et al.* Chiral topological superconductor and half-integer conductance plateau from quantum anomalous Hall plateau transition. *Phys Rev B* 2015; **92**: 064520.
22. He K. MnBi₂Te₄-family intrinsic magnetic topological materials. *npj Quantum Mater* 2020; **5**: 90.
23. Zhao YF, Zhou LJ and Wang F *et al.* Even–odd layer-dependent anomalous Hall effect in topological magnet MnBi₂Te₄ thin films. *Nano Lett* 2021; **21**: 7691–8.
24. Liu S, Yu J and Zhang E *et al.* Gate-tunable intrinsic anomalous Hall effect in epitaxial MnBi₂Te₄ films. *arXiv* 2021; 2110.00540.
25. Liu N, Schreyeck S and Fijalkowski KM *et al.* Antiferromagnetic order in MnBi₂Te₄ films grown on Si(111) by molecular beam epitaxy. *J Cryst Growth* 2022; **591**: 126677.
26. Chen P, Yao Q and Xu J *et al.* Tailoring the magnetic exchange interaction in MnBi₂Te₄ superlattices via the intercalation of ferromagnetic layers. *Nat Electron* 2023; **6**: 18–27.
27. Watanabe R, Yoshimi R and Kawamura M *et al.* Enhancement of anomalous Hall effect in epitaxial thin films of intrinsic magnetic topological insulator MnBi₂Te₄ with Fermi-level tuning. *Appl Phys Lett* 2022; **120**: 031901.
28. Zhu K, Bai Y and Hong X *et al.* Investigating and manipulating the molecular beam epitaxy growth kinetics of intrinsic magnetic topological insulator MnBi₂Te₄ with *in situ* angle-resolved photoemission spectroscopy. *J Phys Condens Matter* 2020; **32**: 475002.
29. Du MH, Yan J and Cooper VR *et al.* Tuning Fermi levels in intrinsic antiferromagnetic topological insulators MnBi₂Te₄ and MnBi₄Te₇ by defect engineering and chemical doping. *Adv Funct Mater* 2021; **31**: 2006516.
30. Chen YL, Chu JH and Analytis JG *et al.* Massive Dirac fermion on the surface of a magnetically doped topological insulator. *Science* 2010; **329**: 659–62.
31. Lee SH, Zhu Y and Wang Y *et al.* Spin scattering and noncollinear spin structure-induced intrinsic anomalous Hall effect in antiferromagnetic topological insulator MnBi₂Te₄. *Phys Rev Research* 2019; **1**: 012011.
32. Suezaki Y and Mori H. Dynamic critical phenomena in magnetic systems. II. *Prog Theor Phys* 1969; **41**: 1177–89.
33. Mazza AR, Lapano J and Meyer III HM *et al.* Surface-driven evolution of the anomalous Hall effect in magnetic topological insulator MnBi₂Te₄ thin films. *Adv Funct Mater* 2022; **32**: 2202234.

34. Shimshoni E and Auerbach A. Quantized Hall insulator: transverse and longitudinal transport. *Phys Rev B* 1997; **55**: 9817–23.
35. Shimshoni E. The quantized Hall insulator: a “quantum” signature of a “classical” transport regime? *Mod Phys Lett B* 2004; **18**: 923–43.
36. Huang Z, Du MH and Yan J *et al.* Native defects in antiferromagnetic topological insulator MnBi₂Te₄. *Phys Rev Materials* 2020; **4**: 121202.
37. Wei HP, Tsui DC and Pruisken AMM. Localization and scaling in the quantum Hall regime. *Phys Rev B* 1985; **33**: 1488–91.
38. van Schaijk RTF, de Visser A and Olsthoorn SM *et al.* Probing the plateau-insulator quantum phase transition in the quantum Hall regime. *Phys Rev Lett* 2000; **84**: 1567–70.
39. Checkelsky JG, Yoshimi R and Tsukazaki A *et al.* Trajectory of the anomalous Hall effect towards the quantized state in a ferromagnetic topological insulator. *Nat Phys* 2014; **10**: 731–6.
40. Kou X, Pan L and Wang J *et al.* Metal-to-insulator switching in quantum anomalous Hall states. *Nat Commun* 2015; **6**: 8474.
41. Khmel'nitskii DE. Quantization of Hall conductivity. *JETP Lett* 1983; **38**: 552–6.
42. Pruisken AMM. Dilute instanton gas as the precursor to the integral quantum Hall effect. *Phys Rev B* 1985; **32**: 2636–9.
43. Kivelson S, Lee DH and Zhang SC. Global phase diagram in the quantum Hall effect. *Phys Rev B* 1992; **46**: 2223–38.
44. Dolan BP. Modular invariance, universality and crossover in the quantum Hall effect. *Nucl Phys B* 1999; **554**: 487–513.
45. Huckestein B. Scaling theory of the integer quantum Hall effect. *Rev Mod Phys* 1995; **67**: 357–96.
46. Wu X, Xiao D and Chen CZ *et al.* Scaling behavior of the quantum phase transition from a quantum-anomalous-Hall insulator to an axion insulator. *Nat Commun* 2020; **11**: 4532.
47. Cai J, Ovchinnikov D and Fei Z *et al.* Electric control of a canted-antiferromagnetic Chern insulator. *Nat Commun* 2022; **13**: 1668.
48. Sass PM, Kim J and Vanderbilt D *et al.* Robust A -type order and spin-flop transition on the surface of the antiferromagnetic topological insulator MnBi₂Te₄. *Phys Rev Lett* 2020; **125**: 037201.

49. Sass PM, Ge W and Yan J *et al.* Magnetic imaging of domain walls in the antiferromagnetic topological insulator MnBi_2Te_4 . *Nano Lett* 2020; **20**: 2609–14.
50. Yasuda K, Mogi M and Yoshimi R *et al.* Quantized chiral edge conduction on domain walls of a magnetic topological insulator. *Science* 2017; **358**: 1311–4.
51. Liu C, Ou Y and Feng Y *et al.* Distinct quantum anomalous Hall ground states induced by magnetic disorders. *Phys Rev X* 2020; **10**: 041063.
52. Garnica M, Otrokov MM and Aguilar PC *et al.* Native point defects and their implications for the Dirac point gap at $\text{MnBi}_2\text{Te}_4(0001)$. *npj Quantum Mater* 2022; **7**: 7.

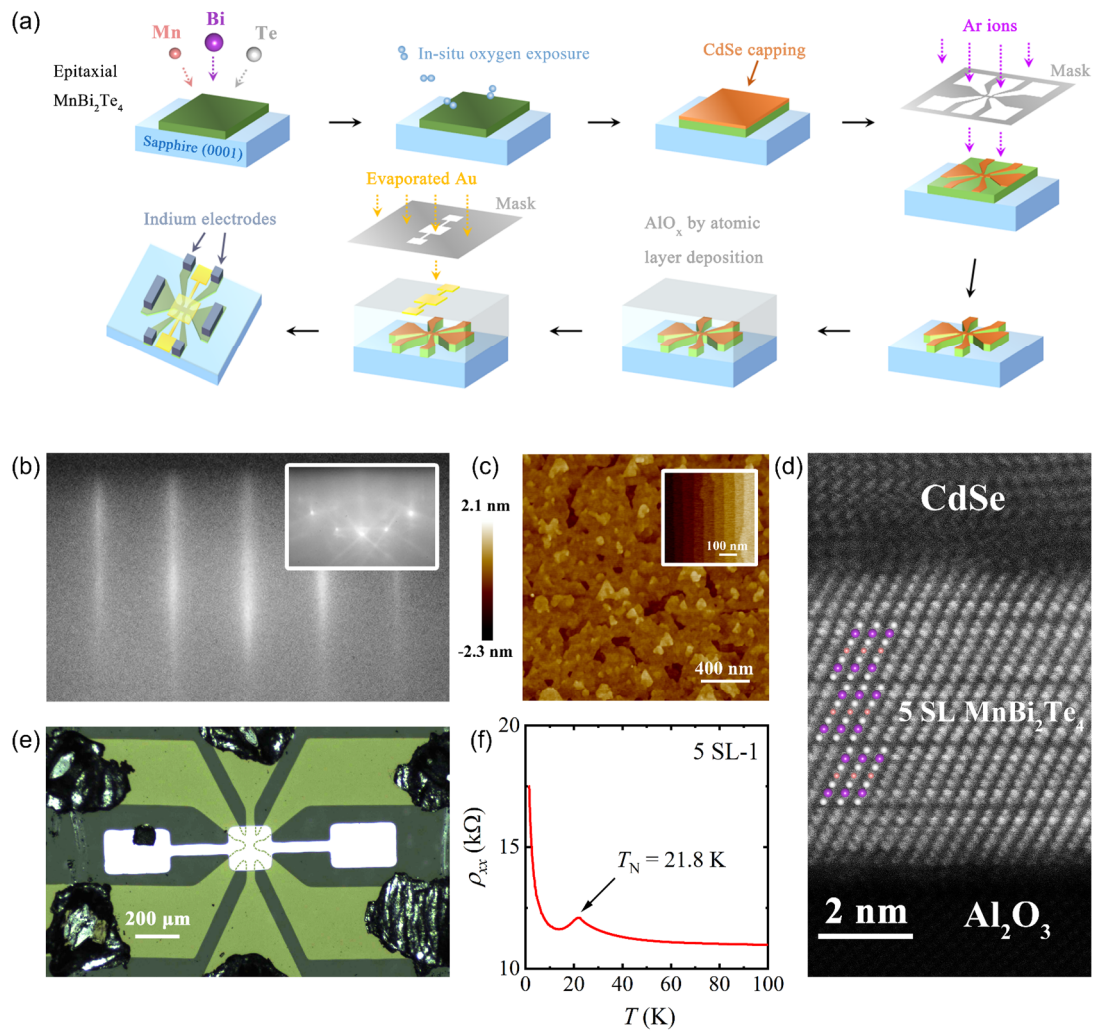


Figure 1. Characterizations of MnBi_2Te_4 thin films. (a) The schematic procedure of sample preparation. (b) RHEED patterns of an as-grown sample and its substrate (inset) in the same direction. (c) Topographies of sample 5 SL-1 with capping layer and a treated substrate (inset). (d) A typical STEM cross-sectional image of a 5-SL sample with same atom colors in (a). (e) Optical microscopy image of a typical device with the Hall bar size of $40 \mu\text{m} \times 80 \mu\text{m}$. The dashed line is guide to eye. (f) The $\rho_{xx}-T$ curve of sample 5 SL-1 with $V_g = 0 \text{ V}$.

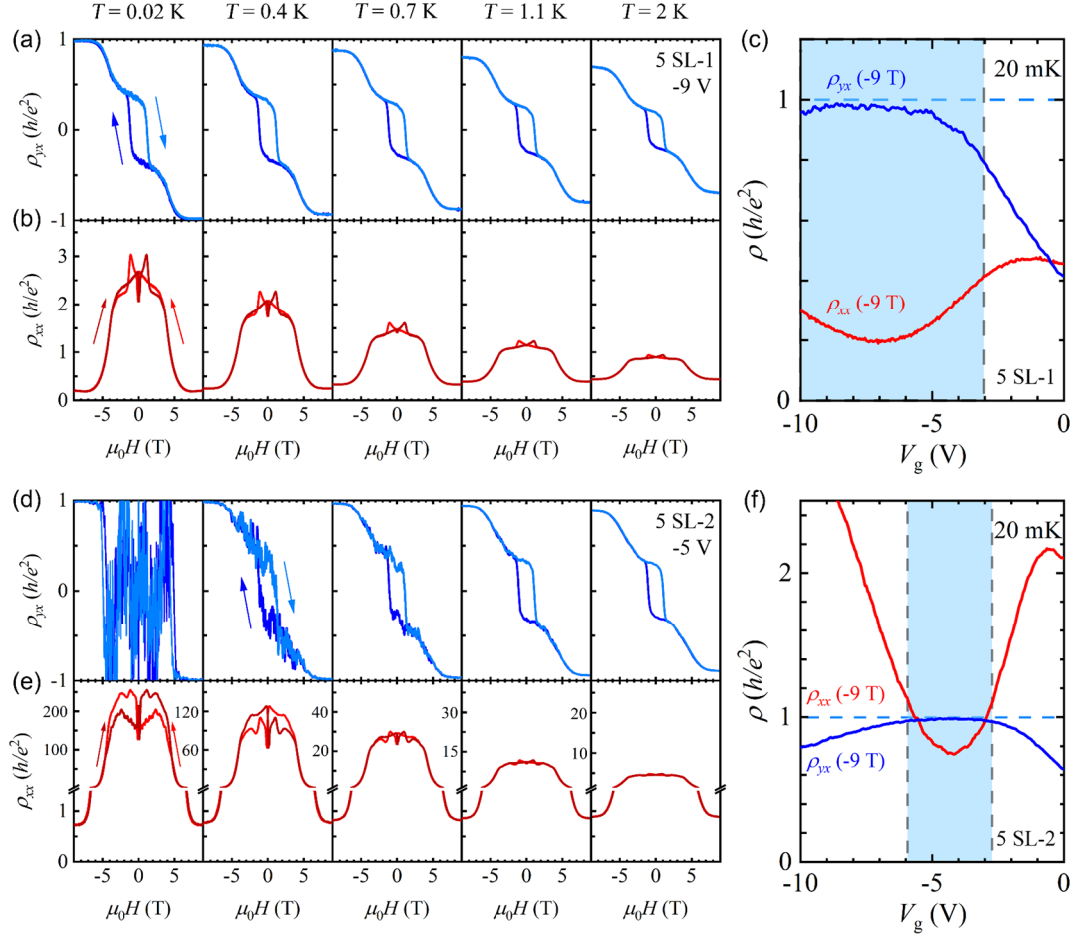


Figure 2. Magneto-transport measurements of 5-SL samples with different post-annealing time. (a, b) The $\rho_{yx}-\mu_0 H$, $\rho_{xx}-\mu_0 H$ curves of sample 5 SL-1 (post-annealed for 30 min.) at selected temperatures below 2 K, respectively. (c) The anti-symmetrized $\rho_{yx}-V_g$ and symmetrized $\rho_{xx}-V_g$ curves of sample 5 SL-1 under -9 T at 20 mK. The colored region represents the area with inverse V_g dependences of ρ_{yx} and ρ_{xx} . (d-f) The transport results of sample 5 SL-2 (post-annealed for 120 min.) with the same measurements as sample 5 SL-1 [corresponding to (a-c) respectively].

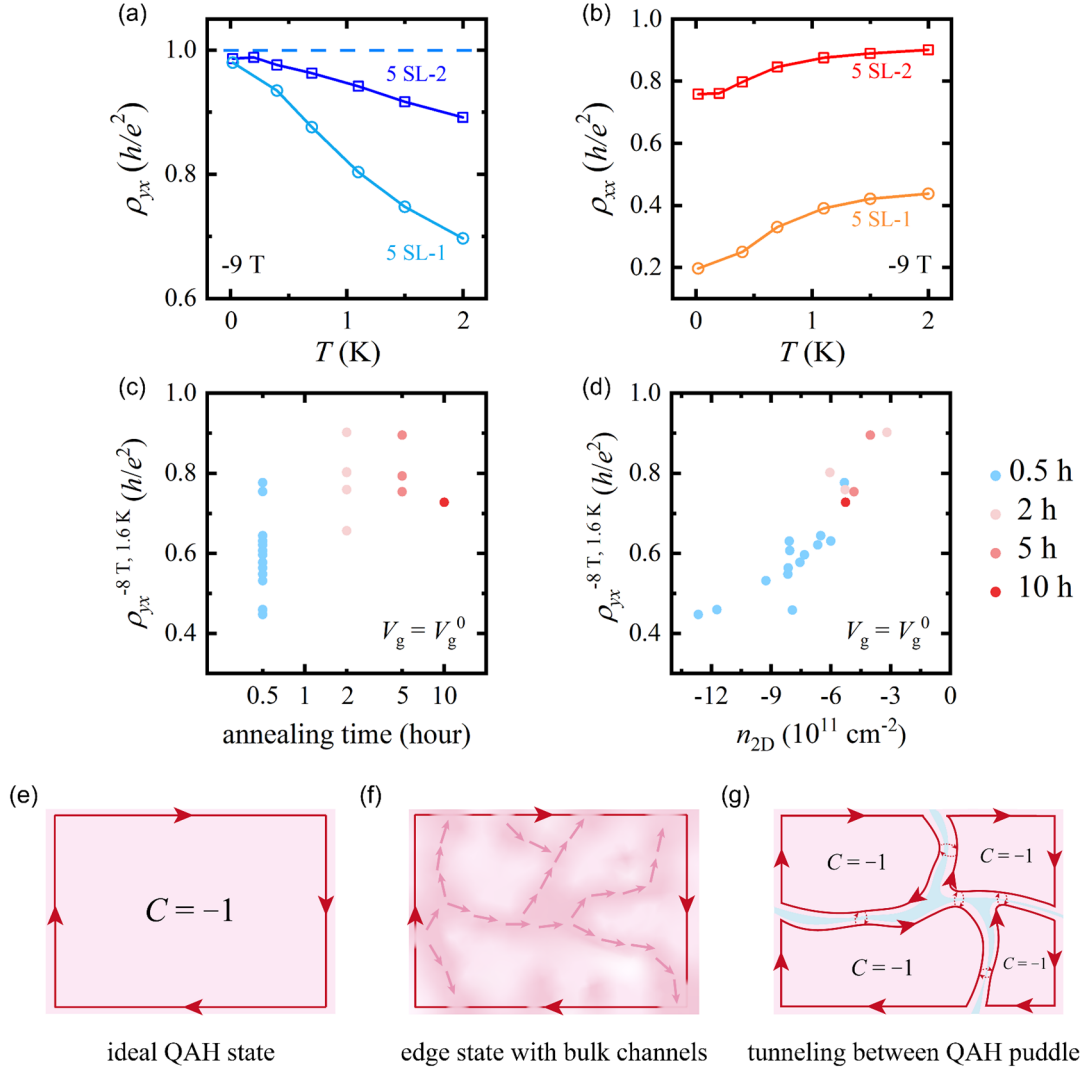


Figure 3. Transport properties of films with different post-annealing time in the ferromagnetic configuration. (a, b) The comparisons of $\rho_{yx}-T$, $\rho_{xx}-T$ curves of samples 5 SL-1 and 5 SL-2 under -9 T at the charge-neutral point, respectively. (c, d) The relations between ρ_{yx} (-8 T) at 1.6 K and post-annealing time, ρ_{yx} (-8 T) at 1.6 K and carrier density (n_{2D}), respectively. All the data are taken at the charge-neutral point ($V_g = V_g^0$) of each sample. (e-g) The schematic of three different scenarios of QAH state in realistic samples. Pink, purple and cyan regions represent QAH insulators, conductive bulk channels (with purple arrows) and insulating regions, respectively. Red solid and dashed lines represent edge states and tunneling processes between edge states, respectively.

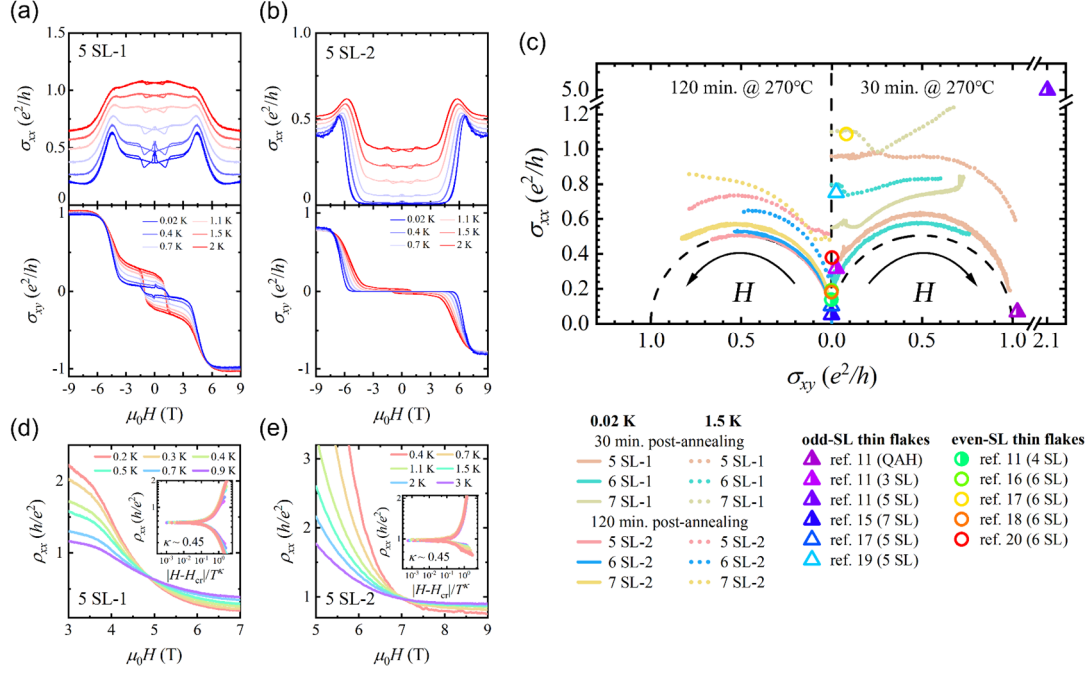


Figure 4. Quantum phase transitions in MnBi_2Te_4 thin films. (a, b) The temperature evolutions of $\sigma_{xx}-\mu_0 H$ and $\sigma_{xy}-\mu_0 H$ curves of sample 5 SL-1, sample 5 SL-2, respectively. (c) Phase diagram depicted by the conductivity tensor. MBE-grown thin films are labeled with different colors. The solid and dotted lines represent the data taken at the base temperature and 1.5 K, respectively. The left and right parts correspond to the data from the long- and short-time post-annealing samples, respectively. Both sides are σ evolutions with increasing magnetic field (indicated by the black arrow). The triangles and circles represent conductivity tensor data of odd- and even-SL exfoliated thin flakes in previous reports around 1.5 K at 0 T, respectively. The aspect ratio of length (L) to width (W) of each device is used to calculate conductivities when they are shown (hollow symbols). If not, $L/W = 1$ is used (symbols colored half). The black dashed semicircle is guide to eye. (d, e) The quantum phase transitions near H_{crs} of sample 5 SL-1, sample 5 SL-2, respectively. The insets show the scaling analyses.